



Universiteit Leiden

DE HAAGSE
HOGESCHOOL

Cavity Ring Down Spectroscopy of Plasma Products



Niels Favier

Cavity Ring Down Spectroscopy of Plasma Products

Student:

Name: Niels Favier

Number: 08015511

Supervisors:

Dr. Joseph Guss

Prof. dr. Harold Linnartz

Coach 1: Dr. Lodewijk Arntzen

Coach 2: Drs. Marlia Vloemans

Committed: Dr. ir. Arno Volker

Abstract

A high resolution infrared spectrum of species formed in a nitrogen-hydrogen plasma expansion was recorded. A cavity ring down detection scheme was used to record a rotationally resolved spectrum in the region from 3300 cm^{-1} to 3380 cm^{-1} . Using the relative intensities and line positions it was determined that the recorded lines belong to the $(1 \leftarrow 0)v_1$, $(1 \leftarrow 0)v_3$, and $(2 \leftarrow 0)v_4$ rotation-vibration spectrum of ammonia at a rotational temperature of $300\text{ K} \pm 30\text{ K}$ with the possibility of other temperature components. Given the high rotational temperature, the ammonia is most likely formed via surface catalysis of plasma products on the inner surface of the vacuum chamber and not in the plasma expansion.

Contents

1. Introduction	1
2. Spectroscopy	2
2.1 Absorption spectroscopy	2
2.2 Cavity ring down spectroscopy	2
2.3 Rotation-vibration spectra	5
2.3.1 Diatomic vibration.....	5
2.3.2 Diatomic rotation.....	7
2.3.3 Polyatomic vibration	8
2.3.4 Polyatomic rotation	10
2.3.5 Rotation-vibration	11
3. Experimental	12
3.1 Gas mixing process.....	12
3.2 Slit jet.....	12
3.3 Plasma.....	13
3.4 Quadrupole mass spectrometer.....	14
3.5 Vacuum system.....	15
3.6 Laser source	16
3.6.1 Pump laser	16
3.6.2 OPO laser	16
3.7 Wave meter and power meter	18
3.8 Acousto-optic modulator	18
3.9 Lenses and pinhole	19
3.10 Optical cavity.....	19
3.11 Scanning and data processing.....	19
4. Cavity ring down spectroscopy measurements	21
4.1 Survey measurements	21
4.2 Relative intensity measurement.....	22
4.3 Relative intensity measurement with added argon	25
5. Discussion	26
5.1 Surface catalysis	26
5.2 Outlook.....	27
6. Conclusion.....	28
7. References	29
8. Appendix	31

1. Introduction

Looking at the night sky, the most obvious objects are stars. These stars and their exo planets form from collapsing clouds of highly dilute matter, the interstellar medium. The interstellar medium mainly consists of gaseous atoms, molecules, ions, and small dust particles and can only be studied by observational research. To assign spectral features, the astronomical observations have to be compared with spectra recorded under laboratory conditions.

Although it is responsible for most of the mass of the observable universe, the interstellar medium is much less dense than any man made vacuum. Many species that would be unstable under atmospheric conditions may be long-lived in the low pressure of the interstellar medium. Studying these unstable species: ions, radicals, cluster ions, and excited species, in the laboratory provides many challenges. Species must be produced under conditions analogous to the interstellar medium, and sustained long enough to be studied. The Sackler laboratory specializes in overcoming these challenges to study molecules and reactions thought to exist in the interstellar medium. One of the set ups used for this work is the supersonic plasma infrared absorption spectrometer (SPIRAS) with which the research in this report is conducted.

One species of interest that has been observed in the interstellar medium is N_2H^+ , this molecular ion has been well studied in the laboratory in the far and mid infrared. In regions where N_2H^+ is present it is likely there are also small amounts of $\text{N}_2\text{H}^+\text{N}_2$ present. This is a special ion, as it bonds the N_2H^+ unit to N_2 through charge transfer. It is known that $\text{N}_2\text{H}^+\text{N}_2$ can be produced in the laboratory but it has been less well studied in the infrared wavelength range. This species is also interesting from a spectroscopic point of view because it is a proton bound dimer. Compared to neutral species, charged species like this are more likely to engage in interactions with other molecules in the interstellar medium. The goal of this research is to record a section of the rotation-vibration spectrum of $\text{N}_2\text{H}^+\text{N}_2$ where a band origin is predicted [1] and assign any observed lines. This will help understand the chemistry that happens in the interstellar medium and may help to predict chemistry for other species.

2. Spectroscopy

This chapter gives an introduction to absorption spectroscopy and discusses its advantages and limitations. The idea of absorption spectroscopy is then expanded by discussing cavity ring down spectroscopy (CRDS). Finally a section is devoted to rotation-vibration transitions of diatomic molecules and then extended to polyatomic molecules.

2.1 Absorption spectroscopy

One of the most basic methods of spectroscopy is absorption spectroscopy. In absorption spectroscopy a light source shines monochromatic light through a sample and a detector measures the intensity of the transmitted light. The relationship between the intensity of the light that hits the sample and the transmitted light is given by the Lambert-Beer law

$$I_t = I_0 e^{-\alpha c_s l_s} \quad (1)$$

in which:

I_t	the transmitted intensity of the light	[W/m ²]
I_0	the light intensity before the sample	[W/m ²]
c_s	the concentration of the sample	[mol/l]
l_s	the length of the sample	[cm]
α	the absorption coefficient	[l·mol ⁻¹ ·cm ⁻¹].

Equation 1 is only valid if certain conditions are met:

- The light is monochromatic
- The sample is homogeneous
- The sample does not scatter the light
- The absorbed light is not reemitted in the same direction
- The concentration of the sample is relatively low.

A spectrum can be made by scanning the wavelength λ and calculating $\alpha(\lambda)$ from the measured intensity values, concentration, and sample length. When either the concentration, the length of the sample, or α is very low and it is not compensated for by one or both of the other factors the signal to noise ratio will be relatively low.

In this research, both the concentration and sample length are limited by the vacuum system i.e. the volume of gas introduced into the vacuum chamber cannot be increased because it would exceed the pumping capacity. Since α is a material constant it cannot be used to compensate for the concentration and sample length.

2.2 Cavity ring down spectroscopy

The sample length can be artificially increased by passing the light through the sample multiple times before measuring the intensity. Sophisticated multi-pass systems allow up to a few dozen passes but require extensive alignment. The light inside the multi-pass system does not follow the same path through the sample on each pass, this is also a disadvantage.

As a solution, consider an empty optical cavity consisting of two highly reflective spherical mirrors. If an infinitely short pulse of light were to be placed in the cavity, a small percentage of the light will be transmitted by the mirrors each time the pulse is reflected. As a result, the intensity of the exiting light follows an exponential decay. The time constant of the decay is mostly determined by the reflectivity of the mirrors and size of the cavity.

If a sample is placed in the cavity, more light will be lost on each round trip due to absorption by the sample. The more light that gets absorbed by the sample, the smaller the time constant of the exponential decay. By measuring the light leaking out of the cavity, the time constant, and thus the absorption coefficient can be determined. This method is called cavity ring down spectroscopy [2]. For one short pulse of light traveling one round trip through the cavity the intensity of the light inside the cavity is depicted in Figure 1.

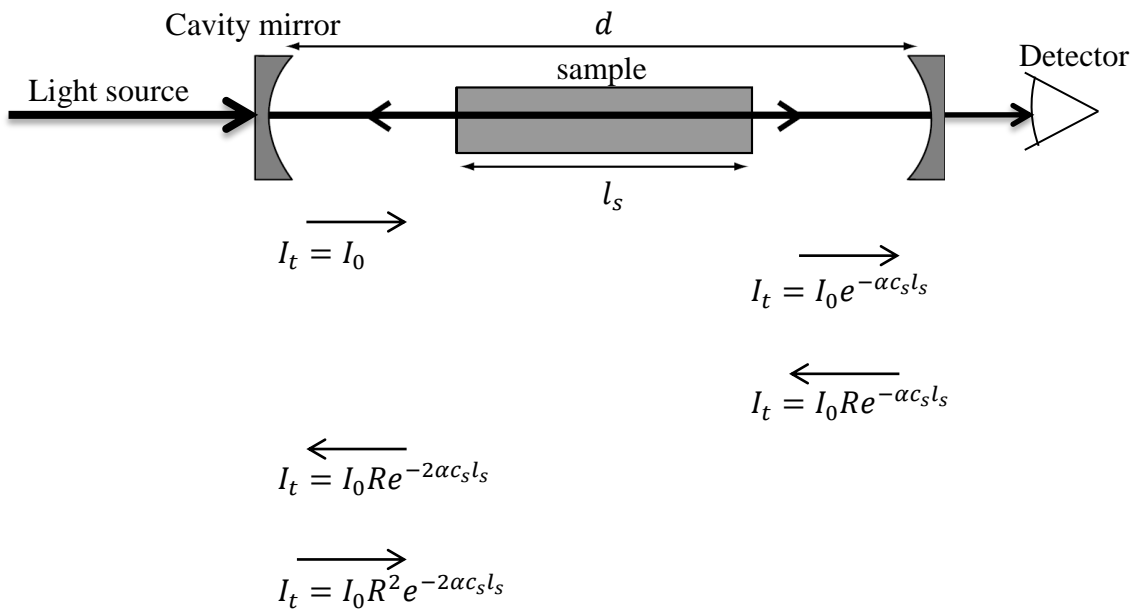


Figure 1 Figure taken from [3] figure 2. Basic optical set up for CRDS, where R is the reflectivity of the mirrors and α is the absorption coefficient of the sample.

For n round trips the intensity of the light equals

$$I_t(n) = I_0 R^{2n} e^{-2n\alpha c_s l_s} \quad (2)$$

in which:

- n a positive integer [-]
- R the reflectivity of the cavity mirrors, typically 0.999 or greater for CRDS [-].

Rewriting equation 2 gives

$$I_t(n) = I_0 e^{-2n(-\ln(R) + \alpha c_s l_s)} \quad (3).$$

Equation 3 is only of use if the light entering the cavity is pulsed and if the pulse does not overlap itself inside the cavity i.e. the length of the pulse must be shorter than twice the cavity length. In a continuous wave system as used here, the discrete variable n needs to be converted to the continuous variable t such that $n = t \frac{c}{2d}$

$$I_t(t) = I_0 e^{-t \frac{c(-\ln R + \alpha c_s l_s)}{d}} \quad (4)$$

in which:

t the time since the light source is turned off at the entry mirror [s]
 d the cavity length [cm]
 c the speed of light [cm/s].

Equation 4 only describes the intensity once no more light is entering the cavity. Equation 4 can be simplified as

$$I_t = I_0 e^{-t/\tau} \quad (5)$$

in which:

τ the ring down time, τ is 2 μ s for an empty 60 cm cavity with $R = 0.999$ [s].

The intensity given by equation 5 is the intensity inside the cavity and is not the same as the intensity measured by the detector. The measured intensity is given by

$$I_m = I_t(t) \cdot e^{-\alpha c_s l_s} \cdot (1 - R) \quad (6)$$

in which:

I_m the measured intensity [W/m²].

Note that the measured intensity follows an exponential decay and that the time constant of the decay depends only on the conditions inside the cavity. The ring down time is given by

$$\tau = \frac{d}{c((1-R) + \alpha c_s l_s)} \quad (7).$$

The absorption coefficient can be extracted from equation 7

$$\alpha = \frac{1}{c_s l_s} \frac{d}{c} \left(\frac{1}{\tau} - \frac{1}{\tau_0} \right) \quad (8)$$

in which:

τ_0 the no sample-absorption ring down time of the spectrum [s].

The baseline value of τ is determined by the cavity length, reflectivity of the mirrors and other optical losses

$$\tau_0 = \frac{d}{c(1-R)} \quad (9).$$

In conclusion, cavity ring down spectroscopy is more sensitive than single pass absorption spectroscopy. For example, in an empty 60 cm cavity with $R = 0.999$, the effective path

length through the cavity is 416 m. Also the effect of laboratory conditions is greatly reduced as CRDS is not dependent on absolute intensities but on the rate of absorption. This means that cavity ring down spectroscopy is not sensitive to power fluctuation of the light source. On the down side, a cavity ring down system is more complex than a regular absorption spectroscopy experiment and requires more extensive alignment.

2.3 Rotation-vibration spectra

There are three main kinds of transitions for molecules, each with their own energy levels and selection rules. Electronic transitions where an electron moves from one electronic state to another, vibrational transitions where the vibrational energy between the different atoms in the molecule changes, and rotational transitions where the rotational energy of the molecule changes. The energies associated with electronic transitions are much greater than vibrational transitions which in turn are much greater than energies associated with rotational transitions. Electronic transitions are too high in energy to be observed in the mid infrared region and will thus not be described here.

A particular transition may involve changes in more than one type of motion. This leads to rotational structure on vibrational transitions and vibrational structures on electronic transitions. Although most of the species of interest are polyatomic, for simplicity diatomic molecules are described here first.

Using the Born-Oppenheimer approximation [4] the motions of the electrons and the nuclei can be considered separately. Because the electrons are very light in comparison to the nuclei, they are assumed to relax instantly to any change in position of the nuclei. In a similar manner the rotational and vibrational motion can be considered separately; this is called the rigid rotor approximation.

2.3.1 Diatomic vibration

For a diatomic molecule, consider the potential energy of a particular electronic state as a function of separation R of the atoms. Due to electrostatic repulsion between nuclei and between electrons, the net force between atoms is repulsive at small R . Most importantly, the Pauli principle provides strong repelling forces between electrons trying to occupy the same space. As R approaches infinity dissociation occurs, this is a process in which the molecule falls apart.

In order to have a bound molecule there must be a region of R where the energy is less than the dissociation energy, see Figure 2. States which do not have a minimum in the potential energy curve will always lead to dissociation.

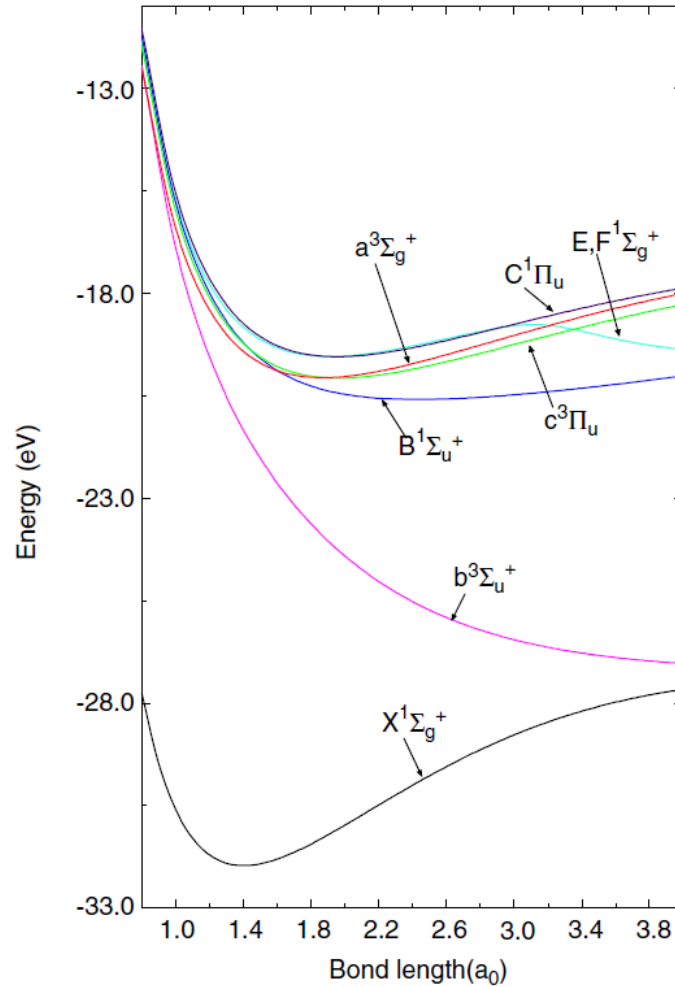


Figure 2 Picture taken from [4] figure 9.2 page 128. The potential energy curves of the seven lowest electronic states of molecular hydrogen, H_2 .

In the case of a potential energy well, the well will be filled with discrete energy levels of vibrational motion. A first approximation for the energy well is a harmonic oscillator. The energy of the vibrational levels in the harmonic oscillator approximation is given by [4]

$$E_v = \omega_e \left(v + \frac{1}{2} \right) \quad (10)$$

in which:

E_v	the energy of the vibrational energy level	$[cm^{-1}]$
ω_e	the harmonic frequency	$[cm^{-1}]$
v	the vibrational quantum number, $v = 0, 1, 2 \dots$	$[-]$.

As can be seen in equation 10 the energy levels in the harmonic oscillator approximation are evenly spaced. The harmonic oscillator approximation can only be used near the bottom of the potential energy well. A more accurate approximation is given by the Morse potential [5]. When using a more realistic curve the energy levels get closer together as the energy increases, becoming a continuum above the dissociation energy, see Figure 3. As is to be expected there are no bound vibrational levels above the dissociation energy.

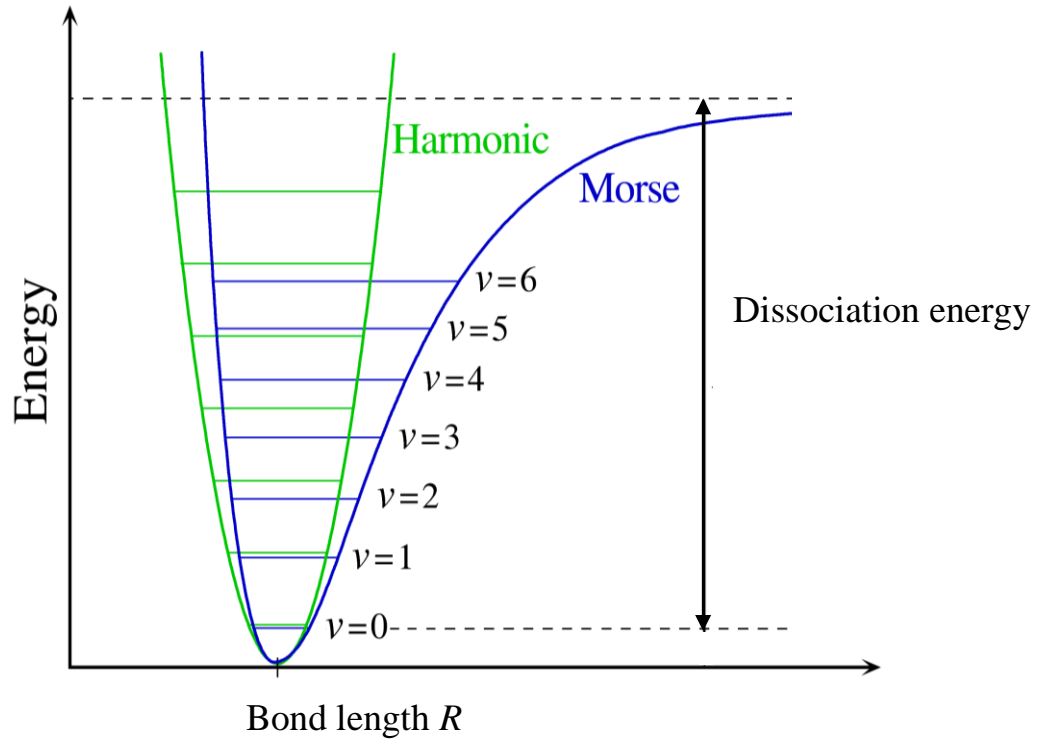


Figure 3 Picture taken from [5]. A Morse potential is a more realistic approximation of the potential energy curve for a diatomic molecule. The vibrational energy levels get closer together as the energy increases and the Morse potential takes the dissociation energy into account.

The Morse potential takes dissociation into account and introduces anharmonicity to the system. This is by approximation represented by an additional term in equation 10

$$E_v = \omega_e \left(v + \frac{1}{2} \right) - \omega_e x_e \left(v + \frac{1}{2} \right)^2 \quad (11)$$

in which:

$\omega_e x_e$ the leading anharmonic correction [cm⁻¹].

All but the electronic transitions need a dipole moment in the molecule for light to be emitted or absorbed. For homo-nuclear diatomics, photo induced vibrational transitions are forbidden because there is no dipole moment.

2.3.2 Diatomic rotation

Within the rigid rotor approximation the energies of the rotational levels are given by [4]

$$E_r = BJ(J + 1) \quad (12)$$

in which:

E_r the energy of the rotational levels [cm⁻¹]
 J rotational quantum number, $J = 0, 1, 2 \dots$ [-]
 B the rotational constant [cm⁻¹].

Where B is inversely proportional to the moment of inertia of the molecule. The general selection rule for dipole allowed rotational transitions is $\Delta J = \pm 1$. Using equation 12 it is then possible to determine the energy of the rotational transitions

$$\Delta E_r = B[J'(J' + 1) - J''(J'' + 1)] \quad (13)$$

in which:

ΔE_r	the energy of the rotational transition	$[\text{cm}^{-1}]$
J'	the J level of the upper state	$[-]$
J''	the J level of the lower state	$[-]$.

Since $\Delta J = \pm 1$ the energy of a rotational transition of a diatomic molecule is given by

$$\Delta E_r = 2BJ' \quad (14).$$

For a diatomic molecule the rotational transitions are, by approximation, regularly spaced by $2B$, see Figure 4.

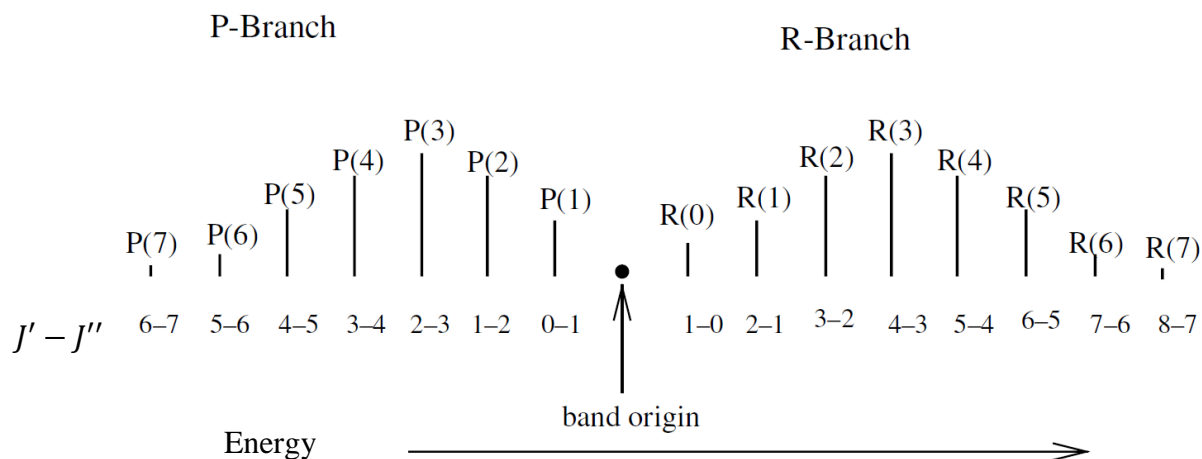


Figure 4 Picture taken from [4] figure 10.8, page 157. Stick spectrum of a diatomic rotation-vibration transition. The band origin, or Q-branch corresponds to $\Delta J = 0$ and is forbidden in the diatomic case. The R-branch corresponds to transitions with $\Delta J = +1$, where R(3) is the transition from $J'' = 3$ to $J' = 4$. The P-branch corresponds to transitions with $\Delta J = -1$, where P(3) is the transition from $J'' = 3$ to $J' = 2$.

The line intensities, as depicted in Figure 4, are largely determined by the rotational temperature of the molecule. The rotational temperature and vibrational temperature are determined by the population of energy levels as given by the Boltzmann distribution. When a molecule is in thermal equilibrium with the surroundings this is equal to the ambient temperature but it may be different for special cases such as in a free-jet expansion. For a low rotational temperature the line intensities for high J values are low, and for low J values the line intensities are high.

2.3.3 Polyatomic vibration

For polyatomic molecules the potential energy curve, as shown in Figure 2, becomes a potential energy surface with $1 + \sum_{i=1}^{N-1} i$ dimensions, where N is the number of atoms in the molecule. There are $3N - 6$ vibrational modes in a non-linear molecule and $3N - 5$ in a

linear molecule. These modes include symmetric stretches, asymmetric stretches and bends, some of which may be degenerate. In a similar way to the diatomic molecules the potential energy wells in the surface are filled with vibrational energy levels. This leads to an approximation of the vibrational energy of the system [4]

$$E_v = \sum_{i=1}^M \left(\omega_i \left(v_i + \frac{1}{2} \right) - \omega_i x_i \left(v_i + \frac{1}{2} \right)^2 \right) \quad (15)$$

in which:

M	the number of vibrational modes	[-]
v_i	the vibrational quantum number of mode i	[-]
ω_i	the harmonic frequency of mode i	[cm ⁻¹]
$\omega_i x_i$	the leading anharmonic correction of mode i	[cm ⁻¹].

Within the harmonic oscillator approximation the selection rule for vibrational transitions is $\Delta v = \pm 1$. In practice any change in v is allowed but $\Delta v = \pm 1$ transitions are much stronger.

Because, for example, the bending vibrational mode behaves very different to the stretching vibrational mode, $\omega_i x_i$ may be either 0, positive, or negative whereas in the diatomic case it is usually positive. A complication in polyatomic molecules is that one vibrational mode may influence another vibrational mode. This requires the introduction of several cross terms, in a triatomic molecule such as H₂O this results in

$$\begin{aligned} E_v = & \omega_1 \left(v_1 + \frac{1}{2} \right) - \omega_1 x_1 \left(v_1 + \frac{1}{2} \right)^2 + \omega_2 \left(v_2 + \frac{1}{2} \right) - \omega_2 x_2 \left(v_2 + \frac{1}{2} \right)^2 \\ & + \omega_3 \left(v_3 + \frac{1}{2} \right) - \omega_3 x_3 \left(v_3 + \frac{1}{2} \right)^2 - x_1 x_2 \left(v_1 + \frac{1}{2} \right) \left(v_2 + \frac{1}{2} \right) \\ & - x_1 x_3 \left(v_1 + \frac{1}{2} \right) \left(v_3 + \frac{1}{2} \right) - x_2 x_3 \left(v_2 + \frac{1}{2} \right) \left(v_3 + \frac{1}{2} \right) \\ & - x_1 x_2 x_3 \left(v_1 + \frac{1}{2} \right) \left(v_2 + \frac{1}{2} \right) \left(v_3 + \frac{1}{2} \right) \end{aligned} \quad (16)$$

in which:

ω_1	the harmonic frequency of mode 1	[cm ⁻¹]
ω_2	the harmonic frequency of mode 2	[cm ⁻¹]
ω_3	the harmonic frequency of mode 3	[cm ⁻¹]
v_1	the vibrational quantum number of mode 1	[-]
v_2	the vibrational quantum number of mode 2	[-]
v_3	the vibrational quantum number of mode 3	[-]
$\omega_1 x_1$	the leading anharmonic correction of mode 1	[cm ⁻¹]
$\omega_2 x_2$	the leading anharmonic correction of mode 2	[cm ⁻¹]
$\omega_3 x_3$	the leading anharmonic correction of mode 3	[cm ⁻¹]
$x_1 x_2$	the anharmonic cross term for mode 1 and 2	[cm ⁻¹]
$x_1 x_3$	the anharmonic cross term for mode 1 and 3	[cm ⁻¹]
$x_2 x_3$	the anharmonic cross term for mode 2 and 3	[cm ⁻¹]
$x_1 x_2 x_3$	the anharmonic cross term for mode 1, 2, and 3	[cm ⁻¹].

Although usually positive, the cross terms may be either 0, positive, or negative. In most molecules the anharmonicity causes the energy levels to get closer together as the energy increases. For molecules with more than 3 atoms, the number of cross terms grows exponentially with the number of atoms.

2.3.4 Polyatomic rotation

Regarding polyatomic molecules the rotational energy can only be solved for certain configurations. For linear molecules such as HCN, equation 12 can be used.

The rotational motion of polyatomic molecules with other configurations is complicated as there are several axes about which rotation may occur. The principle axes are the orthogonal axes where the moment of inertia about the a axis, I_A , is the smallest possible and the moment of inertia about the c axis, I_C , is the largest possible. The value of the moment of inertia along the b axis is $I_A \leq I_B \leq I_C$. When rotation about the different axes is considered separately, the rotational constant introduced in equation 12 needs to be split into three constants, one for each principle axis:

$$A = \frac{h}{8\pi^2 c I_A} \quad (17)$$

$$B = \frac{h}{8\pi^2 c I_B} \quad (18)$$

$$C = \frac{h}{8\pi^2 c I_C} \quad (19)$$

in which:

A	the rotational constant about the a axis	$[\text{cm}^{-1}]$
B	the rotational constant about the b axis	$[\text{cm}^{-1}]$
C	the rotational constant about the c axis	$[\text{cm}^{-1}]$
h	Planck's constant	$[\text{g}\cdot\text{cm}^2/\text{s}]$
I_A	the moment of inertia about the a axis	$[\text{g}\cdot\text{cm}^2]$
I_B	the moment of inertia about the b axis	$[\text{g}\cdot\text{cm}^2]$
I_C	the moment of inertia about the c axis	$[\text{g}\cdot\text{cm}^2]$.

In the case of non-linear molecules the rotational energy can only be solved in two cases: a prolate symmetric top (similar to a cigar in shape) where $B = C$ and an oblate symmetric top (similar to a wheel in shape) where $A = B$. The energy of the rotational structure for a prolate symmetric top can be approximated by

$$E_r = BJ(J + 1) + (A - B)K^2 \quad (20)$$

in which:

K the projection of J on the unique axis, K has integer values from $-J$ to $+J$ [-].

The energy of the rotational structure for an oblate symmetric top can be approximated by

$$E_r = BJ(J + 1) + (C - B)K^2 \quad (21).$$

Selection rules for J and K are largely dependent on the symmetry in the molecular frame and orientation of the dipole moment with respect to the principle axes.

2.3.5 Rotation-vibration

When vibrational states are combined with rotational states in a diatomic molecule the energy can be estimated as follows [4]

$$E_{VR} = \omega_e \left(v + \frac{1}{2} \right) + B_e J(J + 1) - \omega_e x_e \left(v + \frac{1}{2} \right)^2 - D_e J^2(J + 1)^2 - \alpha_e \left(v + \frac{1}{2} \right) J(J + 1) + \dots \quad (22)$$

in which:

E_{VR}	the energy of a particular rotation vibrational level	[cm ⁻¹]
D_e	the centrifugal distortion	[cm ⁻¹]
α_e	the variation of B_e with the vibrational state	[cm ⁻¹].

Equation 22 is a descriptive formula where the constants are empirically derived from measurements. Needless to say the rotation-vibration spectrum for polyatomic molecules is much more complicated than that of diatomic molecules. As mentioned earlier the vibrational and rotational transitions need a dipole moment for photo-induced transitions. In the case of linear molecules such as CO₂, dipole allowed transitions are only possible when the molecule is bent or asymmetrically stretched due to vibrations.

3. Experimental

This chapter discusses the SPIRAS experimental set up. Briefly: molecular nitrogen gas and molecular hydrogen gas are mixed and injected into the main vacuum chamber via a free-jet expansion slit. Molecules of interest are formed inside a plasma, some of which enter the quadrupole mass spectrometer (QMS) for further analysis.

The free-jet expansion crosses an optical cavity such that the light passes through the gas orthogonal to the gas flow direction. A tunable light source is used for this purpose. In order to collect the ring down time an optical switch is necessary, for this purpose an acousto-optic modulator (AOM) is used. An infrared (IR) detector is used to measure the light leaking from the cavity.

3.1 Gas mixing process

A mixing line is used to mix the gas supplied from several gas cylinders to the correct ratio. It is possible to connect up to four gas cylinders to the mixing line and each has its own closing valve and needle valve. The needle valves and the regulators on the gas cylinders are used to control both the ratio of the gas mixture as well as the total pressure in the gas mixing line. The running pressure in the mixing line is typically 400 mbar but may be as low as 300 mbar or as high as 600 mbar depending on the status of the plasma.

In the scope of this report only species consisting of nitrogen and hydrogen atoms or ions are of interest. Therefore one gas cylinder containing molecular nitrogen (N_2), of purity 3.0, and one gas cylinder containing molecular hydrogen (H_2), of purity 2.5, are connected to the gas mixing line. The contribution of the hydrogen to the total pressure in the mixing line is typically 5 mbar to 60 mbar.

3.2 Slit jet

The gas mixture is continuously injected into the main vacuum chamber via a narrow slit. The slit is connected to the mixing line via a valve and forms a 'free-jet expansion' [6] in the vacuum chamber. As the molecules exit the slit, a small fraction is converted to other molecules, ionic complexes, and other radicals in a plasma (see next section). Because of the high pressure in the mixing line relative to that in the vacuum chamber many collisions occur in this region.

The likelihood of a collision between two plasma-formed species is low with respect to the likelihood of a collision between a plasma-produced molecule and a carrier gas molecule. Collisions between plasma-produced species and carrier gas molecules convert rotational energy of the plasma-produced species into translational energy of the carrier gas molecule. This should cause the plasma-produced molecules to be rotationally cold, 20 K to 100 K, this should then result in relatively simple spectra, with only lower J values being populated.

Further into the main vacuum chamber the jet expands to a point where very few collisions occur and the molecules all travel in approximately the same direction, this region is called the 'zone of silence', see Figure 5. The laser beam is directed through the zone of silence orthogonal to the direction of the gas expansion and parallel to the slit.

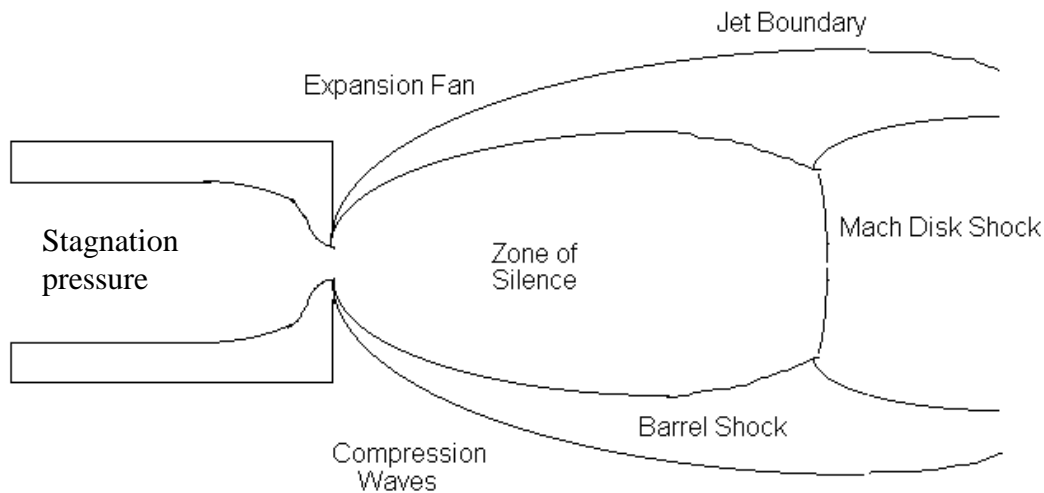


Figure 5 Picture taken from [6]. Schematic representation of the free-jet expansion.

The slit is 32 mm by 50 μm , typical pressures in the vacuum chamber are 0.1 mbar when the gas is flowing into the main chamber and $5 \cdot 10^{-3}$ mbar when there is no gas flow. One final feature of the free-jet expansion is that the velocity distribution orthogonal to the gas flow direction is very small, resulting in line widths with very small Doppler broadening. Doppler broadening is a process in which lines in an optical spectrum are broadened by the red- and blue-shifted absorptions of molecules moving away from and towards the incident photons respectively.

3.3 Plasma

A plasma is a state of matter similar to the gas phase in which electrons move freely and some amount of molecules is ionized. This is accompanied by the dissociation of molecules and creation of ionic complexes and other radicals. When a large enough portion of molecules in a gas is ionized, a plasma is created. Due to the large number of ions and free electrons in the plasma it is electrically conductive, unlike materials in the gas phase.

To produce a plasma in SPIRAS, a beam of electrons is guided through the expanding gas. The final products of the plasma are numerous species, several of which are charged. Adjusting gas pressures, relative position of the electron beam with respect to the free-jet expansion, and current through the filament, the plasma can be optimized for certain species. Note that the plasma is often unstable and changes shape or brightness, from day to day it might require a slightly different current and pressure to be stable. This results in an uncertainty in the production efficiency of target species and therefore in the intensity of any observed lines.

The electron beam is produced by directing thermally emitted electrons towards the free-jet expansion. The electrons are emitted by a tungsten filament (0.2 mm in diameter) through which a current between 3.2 A and 4.5 A runs, depending on the status of the plasma. The filament is surrounded by a slotted molybdenum tube and both are electrically isolated from the mount they are held in. Also, both the filament and the molybdenum tube are set at a bias

voltage of -120 V (see Figure 6) causing the electrons to be accelerated towards the grounded shield in a planar beam.

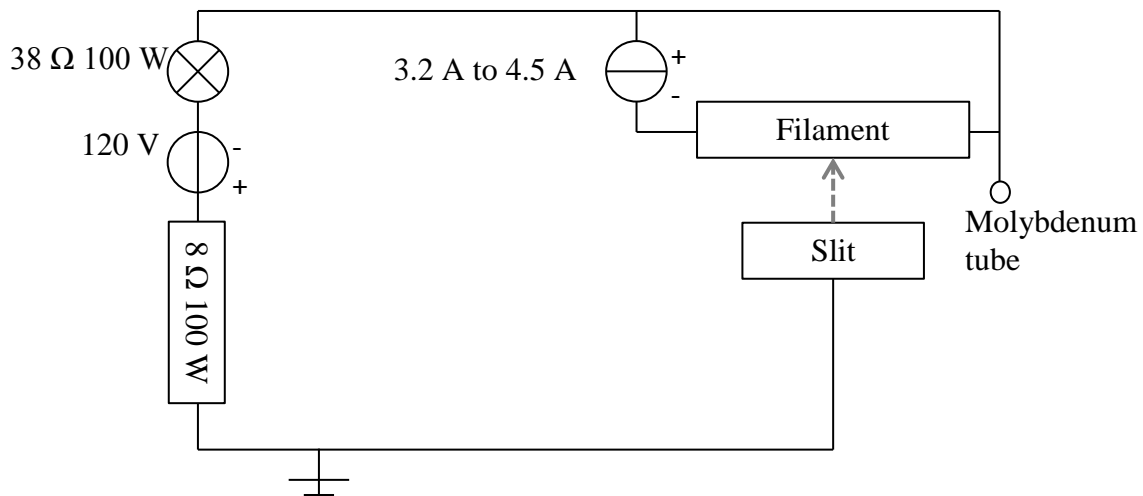


Figure 6 Schematic representation of the circuit diagram for the filament, molybdenum tube, slit and light bulb.

The grounded shield has a slot with the same dimensions as that of the molybdenum tube and is placed in front of the molybdenum tube, see Figure 7.

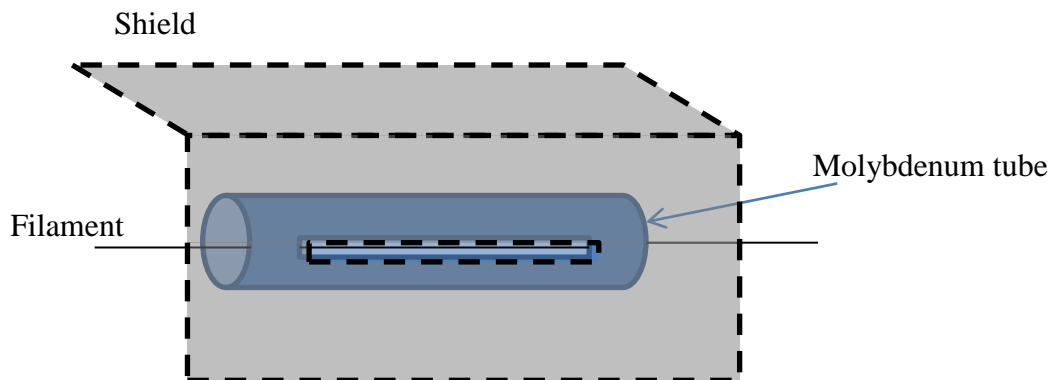


Figure 7 Schematic representation of the filament, molybdenum tube and shield.

If aligned properly the beam passes through the shield towards the free-jet expansion. Once plasma has struck, a current runs through a light bulb indicating the plasma has struck. To prevent any discharge of the plasma onto the cavity mirrors, helium curtains are made by spraying helium gas along the mirrors. The added helium does not affect the produced spectrum because helium is transparent at these wavelength ranges.

3.4 Quadrupole mass spectrometer

A QMS is used to optimize plasma conditions for specific species such as $N_2H^+N_2$. The QMS (Balzers model QMG 511) is contained within a separate vacuum chamber mounted within the main chamber and is pumped using a diffusion pump and fore pump in sequence. Typical running pressures in the QMS vacuum chamber are in the order of $1 \cdot 10^{-6}$ mbar. Using a skimmer placed at the end of the zone of silence, a small sample of the produced species

enters the QMS vacuum chamber while the rest of the gas is evacuated using the regular vacuum system. The skimmer consists of a conical piece of metal with a 200 μm orifice at the tip of the cone.

A quadrupole field is formed between four parallel electrically conducting rods, see Figure 8. A pair of oppositely placed rods is held at a positive bias voltage, the other pair is held at a negative bias voltage of equal magnitude. A radiofrequency oscillator then adds a high frequency voltage to the first pair and adds the same signal with a 180° phase shift to the other pair of rods.

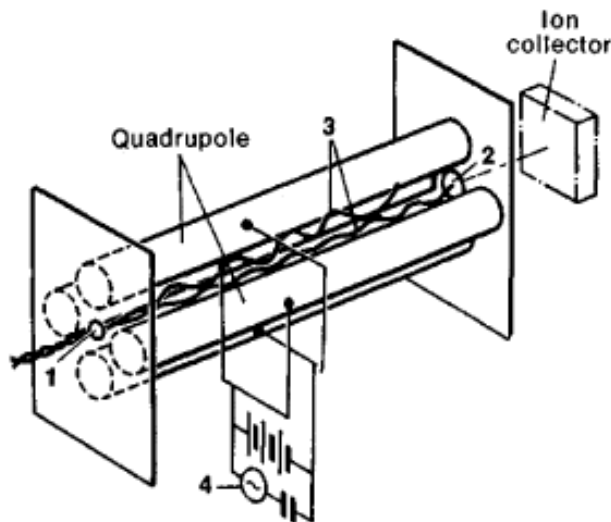


Figure 8 Picture taken from [7] figure 7. Schematic representation of a quadrupole mass spectrometer. 1: the beam of ions enters the mass spectrometer. 2: the beam exits the mass spectrometer to be collected at the ion collector. 3: ions of the wrong m/z are dissipated from the mass spectrometer. 4: by scanning the frequency of the high frequency signal, a mass spectrum can be obtained.

An ion that enters the field parallel to the rods will start to oscillate as it moves further between the rods. If the ion has the right m/z with respect to the bias voltage and the frequency of the signal it will move through the quadrupole field and it is detected at the other end of the rods. Other ions will oscillate with increasing amplitude until they become dissipated from the mass spectrometer. By scanning the frequency of the high frequency signal, a mass spectrum can be obtained. The QMS in SPIRAS is only capable of detecting cations.

3.5 Vacuum system

A small mechanical pump is used to get the QMS chamber from atmospheric pressure to $3.5 \cdot 10^{-2}$ mbar after which the diffusion pump takes over. Typical pressures without gas flow through the slit are $4 \cdot 10^{-6}$ mbar and with gas flow $7 \cdot 10^{-6}$ mbar.

The main chamber is pumped using two roots blower pumps (approximately $4000 \text{ m}^3/\text{h}$) and one fore pump ($80 \text{ m}^3/\text{h}$) in sequence. The pumps are connected to the main chamber via a large tube which can be closed at both ends using a gate valve at the pump end and a butterfly valve at the main chamber end. The butterfly valve has a smaller bypass channel and valve attached to it. This is because if the butterfly valve is opened suddenly the QMS skimmer can be damaged by the sudden shockwave. When the pressure in the main chamber is in the order of 10 mbar and the pressure in the tube is in the order of 1 mbar it is safe to slowly open the

butterfly valve. Typical pressures, without injecting gas into the main chamber are around $5 \cdot 10^{-3}$ mbar and 0.1 mbar with gas flow.

3.6 Laser source

The light source consists of a fiber amplifier-pumped optical parametric oscillator (OPO) laser system which results in a tunable light source. Briefly: the pump laser sends a laser beam with a wavelength of approximately 1064 nm to the OPO laser which converts the light to the target wavelength. Three stages of tuning are possible: translating the crystal inside the OPO laser will change the wavelength in steps of approximately 13 cm^{-1} , rotating an intracavity etalon inside the OPO laser changes the wavelength with steps of approximately 1 cm^{-1} , or varying the strain on the pump diode laser which results in a continuous wavelength variation.

3.6.1 Pump laser

The laser used to pump the OPO laser is a fiber amplifying laser (IPG Photonics model YAR-10K-1064-LP-SF) with a wavelength of 1064 nm. The laser consists of two major components: a seed diode laser and a fiber amplifier. The seed laser is coupled into the fiber amplifier where the power is amplified to 10.0 W and sent to the OPO via a fiber optic cable.

The finest wavelength tuning of the optical system is performed within the seed laser. A piezo element is attached to the seed laser, when a voltage is applied to the piezo element it compresses the diode laser resulting in a continuous wavelength change. This allows the wavelength to be scanned with a range up to 1.2 cm^{-1} . The voltage is controlled by a custom LabVIEW program.

3.6.2 OPO laser

For further wavelength tuning an OPO laser (Aculight Argos model 2400 CW OPO wavelength module B) is used. The OPO converts the pump laser beam into two laser beams with lower energy, the signal and idler beam. The conversion takes place inside a specially constructed crystal. The crystal is composed of many oppositely poled layers with increasing thickness in the y direction, see Figure 9. The relation between the wavelengths of the different laser beams is as follows

$$\frac{1}{\lambda_p} = \frac{1}{\lambda_s} + \frac{1}{\lambda_i} \quad (23)$$

in which:

λ_p	the wavelength of the pump laser beam	[m]
λ_s	the wavelength of the signal laser beam	[m]
λ_i	the wavelength of the idler laser beam	[m].

Note that there is conservation of energy in equation 23 as the wavelength of the light is inversely proportional to the energy.

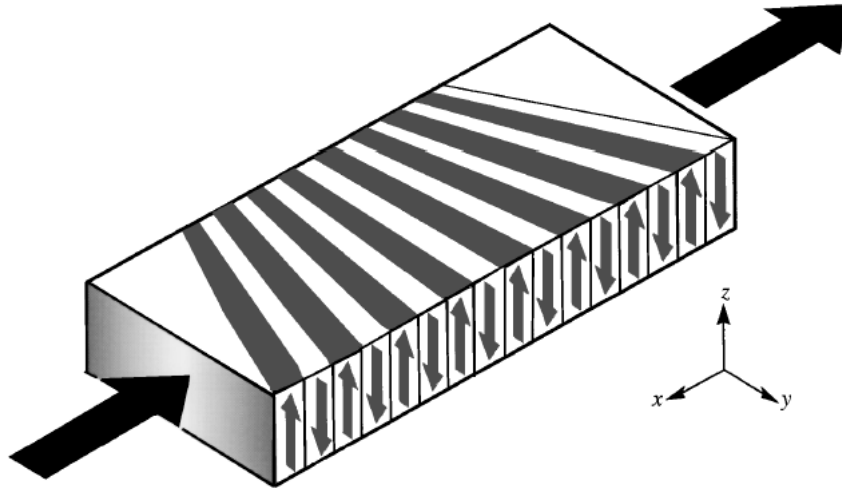


Figure 9 Picture taken from [8] figure 1. Exaggerated depiction of the fan out structure of the crystal inside the OPO. The arrows on the side of the crystal indicate the poling direction. The different laser beams travel along the x axis.

The conversion is done via quasi phase matching [8], the three waves overlap inside the crystal and are all harmonics of the poling period. The signal beam resonates within the optical cavity in which the crystal is contained, see Figure 10. The idler beam is coupled out of the cavity to be used in CRDS while the signal beam induces more conversion on each round trip through the cavity. By moving the crystal in the y direction with respect to the pump beam, the poling period changes. This in turn will change the wavelengths of the signal and idler beam. The wavelength of the idler beam can be changed in steps of approximately 13 cm^{-1} using the crystal position.

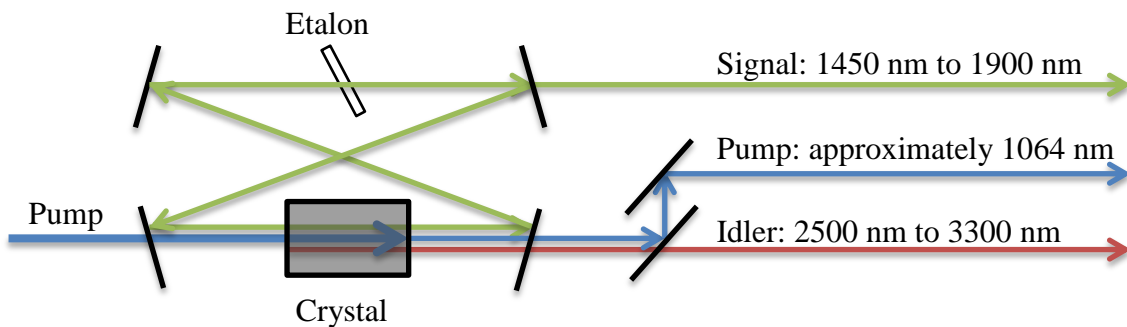


Figure 10 Schematic representation of the crystal, etalon and optical cavity. For clarity, overlapping beams have been separated.

Also contained within the optical cavity is an etalon, this is a small transparent plate. Depending on the angle of the etalon with respect to the laser beam, the reflections from the two surfaces of the etalon will interfere constructively for a certain mode of the signal beam. By changing the angle of the etalon one can favor a certain mode of the signal beam which in turn favors a certain mode in the idler beam. The wavelength can be changed in a range of up to 14 cm^{-1} in steps of approximately 1 cm^{-1} .

3.7 Wave meter and power meter

To monitor the output of the OPO, a wave meter (Bristol 621 wavelength meter) and power meter (Thorlabs model S310C) are used, see Figure 11. Via a beam splitter 1% of the idler beam is directed into the wave meter. The remaining beam is sent into a power meter which is removed during CRDS measurements. Both the wave meter and power meter can be read by the LabVIEW program.

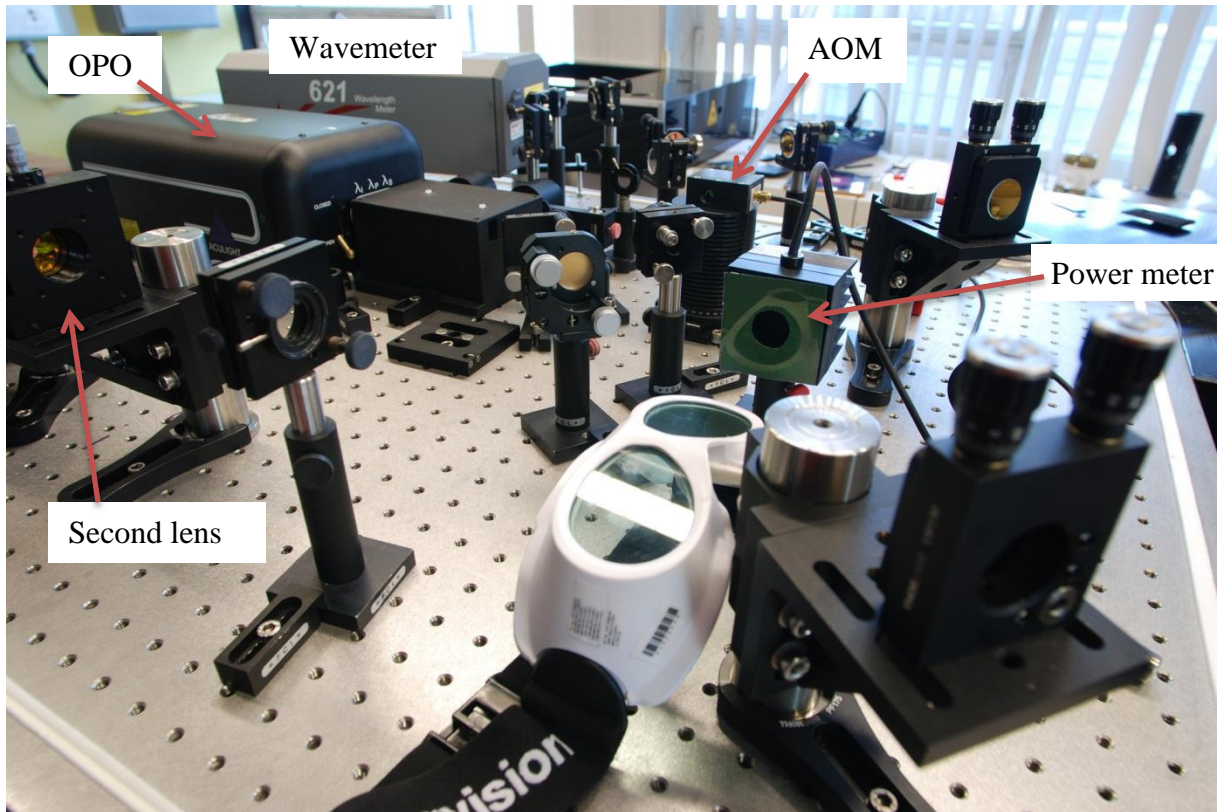


Figure 11 Photograph of the optical part of the setup, the power meter has been removed from the beam path.

3.8 Acousto-optic modulator

Once light is coupled into the optical cavity and has built up to a threshold value, the beam must be blocked rapidly. For this purpose an AOM (ISOMET model 1210) is incorporated in the setup, see Figure 11. The AOM consists of a germanium crystal with a piezo attached to the side, a high frequency (80 MHz) voltage is applied to the piezo element so compression waves travel through the crystal. When active, the AOM splits an incident laser beam into a fundamental and a 1st order beam, where the 1st order beam is emitted under a slight angle from the incident beam and with a frequency increased by 80 MHz. When the AOM is not active only the fundamental beam remains, this way the AOM can be used as an optical switch. When the AOM is active the cavity is filled with light, when threshold is reached it is turned off. The typical reaction time between threshold and the beam being stopped is 750 ns. Also, by adjusting the amplitude of the high frequency voltage, the power of the 1st order beam can be controlled.

3.9 Lenses and pinhole

The cavity can support multiple modes, usually one Gaussian TEM₀₀ mode and several higher order transverse modes each with their own ring down times. Preferably, only the TEM₀₀ mode is excited, this can be achieved by matching the waist size and location of the laser beam to the waist size and location of the TEM₀₀ cavity mode [3]. A system of two lenses and a pinhole is used for this purpose. The first lens is placed after the AOM and focusses the laser onto a 150 μm pinhole. The second lens images the pinhole at the center of the cavity, at the correct waist size. The two final mirrors before the cavity are then used to direct the beam into the cavity under the correct angle and at the right position for the TEM₀₀ mode.

3.10 Optical cavity

The cavity itself consists of two spherical mirrors (Novawave) placed 54 cm apart at opposing sides of the vacuum chamber. The reflectivity of the mirrors is 99.97% at 3.3 μm. The high finesse optical cavity created by the mirror pair imposes strict selection criteria on light entering. Therefore a piezo element is attached to one of the mirrors. A triangle wave signal with a frequency of 20 Hz is applied to the piezo element. For a brief moment during the rise and fall of the signal, when the cavity length is a harmonic of the laser wavelength, the beam will be able to resonate in the cavity and a ring down can be recorded.

3.11 Scanning and data processing

To record a ring down, the intensity of the light leaking from the cavity is measured with an IR detector (VIGO system model PVI-3TE-5 type MIPAC-F-50). Once the intensity reaches a certain threshold, a trigger is sent to the AOM which switches off the light entering the cavity. Once no more light enters the cavity, the light leaking from the cavity undergoes an exponential decay. The decay is recorded by the IR detector and read using a data acquisition card. Using a custom LabVIEW program an exponential decay is fitted to the ring down where the time constant is τ .

Each point in a scan is the average τ of several ring downs, for a survey scan this would be 5 ring downs per point, for a normal scan 15 ring downs per point. Once a point is recorded the voltage applied to the piezo attached to the seed laser is decremented by a predetermined step size, usually 0.05 V which corresponds to a step size of $0.6 \cdot 10^{-3} \text{ cm}^{-1}$. The wavelength of the light is recorded every 10 points, at the end of the scan the recorded values are saved.

During a scan, the crystal position and etalon angle are fixed, the only wavelength control used to scan the wavelength is the voltage of the piezo attached to the seed laser. This limits the length of the scan to 1.2 cm^{-1} at best, therefore any longer spectra are built up from multiple smaller overlapping scans. A 1.2 cm^{-1} scan takes approximately 20 minutes, this means some of the longer spectra consist of measurements taken on different days. Because of the unpredictability of the plasma from day to day, the relative intensities of broadly spaced lines should be treated as indicative rather than absolute.

Using the QMS, the plasma is first optimized for the species of interest prior to a measurement session. Due to a malfunction in the QMS, this was only possible for the measurements taken before the 15th of March. Without QMS, the presence of the species of

interest can be checked by scanning a few previously recorded lines of the infrared spectrum using CRDS. This method is less accurate than using the QMS since the assumption is used that all lines belong to the same species.

The wavelength measurements and τ measurements are combined to plot τ as a function of the wavelength. Then τ_0 is drawn on the plot and, using equation 8, the ring down time is converted to α . Note that because no real concentration is used this is not the actual value of α but is linearly scaled to it, for clarity α_s is used when the concentration is not taken into account.

4. Cavity ring down spectroscopy measurements

This chapter displays the results of measurements undertaken to record the spectrum of the species of interest. The observed lines are assigned and measurements concerning the rotational temperature are carried out.

4.1 Survey measurements

To investigate the predicted [1] section in the spectrum, a survey is done from 3381.5 cm^{-1} to 3299.5 cm^{-1} . An average of 5 ring downs per point is used and a 5 point adjacent average smoothing is applied. The survey of the spectrum is shown in Figure 12.

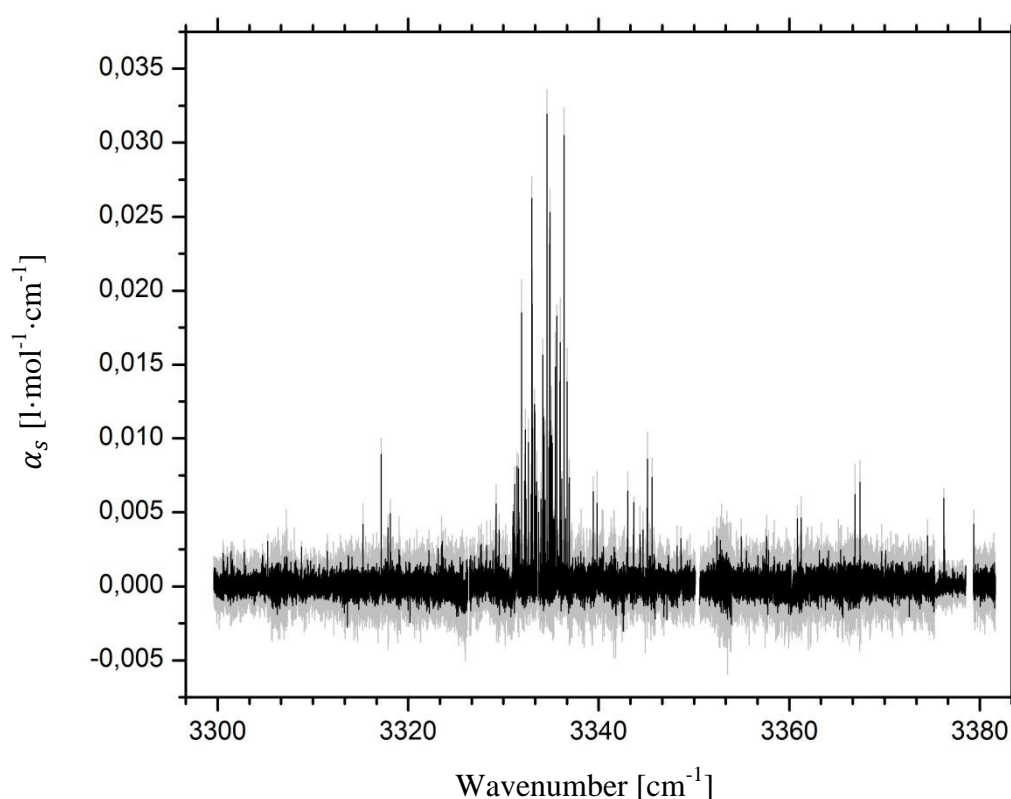


Figure 12 A survey of the spectrum from 3381.5 cm^{-1} to 3299.5 cm^{-1} . Each point is the average of 5 ring downs and converted to α_s , displayed in grey. Then a 5 point adjacent average smoothing is applied, displayed in black.

As suggested in [9] subsequent $\text{N}_2\text{H}^+\text{N}_2$ lines should be roughly 0.16 cm^{-1} apart and the full spectrum should show a P-R band structure, this is clearly not the case. The region from 3331 cm^{-1} to 3337 cm^{-1} has a much larger line density than other regions of the spectrum.

4.2 Relative intensity measurement

In order to determine to which species the lines belong a more accurate measurement of the region from 3331 cm^{-1} to 3337 cm^{-1} is necessary. If a more accurate measurement can be performed during a single session the relative intensities can be used to identify potential species.

A measurement is performed from 3330.5 cm^{-1} to 3337 cm^{-1} during a single session. The total pressure in the mixing line was kept at 400 mbar, 40 mbar of which is molecular hydrogen. 15 ring downs per point are used and a 5 point adjacent average smoothing is applied, see Figure 13. Gaussians are fitted to each peak using the unsmoothed data, the formula for a Gaussian is

$$y(x) = y_0 + \frac{A}{W\sqrt{\frac{\pi}{2}}} e^{-2\left(\frac{x-x_c}{W}\right)^2} \quad (24)$$

in which:

A	the area under of the Gaussian	$[\text{l}\cdot\text{mol}^{-1}\cdot\text{cm}^{-2}]$
W	the width of the Gaussian	$[\text{cm}^{-1}]$
x_c	the center wavelength of the Gaussian	$[\text{cm}^{-1}]$
x	the wavelength	$[\text{cm}^{-1}]$
y_0	the baseline value of the Gaussian	$[\text{l}\cdot\text{mol}^{-1}\cdot\text{cm}^{-1}]$
$y(x)$	the height of the Gaussian at x	$[\text{l}\cdot\text{mol}^{-1}\cdot\text{cm}^{-1}]$.

All recorded line positions and fit parameters are listed in Table 2 in the appendix. Using this spectrum, many lines have been assigned to be part of the $(1 \leftarrow 0)v_1$ and $(1 \leftarrow 0)v_3$ Q-branch of ammonia (NH_3) [10]. A systematic offset of $0.037 \text{ cm}^{-1} \pm 0.003 \text{ cm}^{-1}$ in the line positions with respect to the positions listed in [10] is found, where the observed lines are lower in energy. Presumably this is due to a systematic offset in the wave meter. The corrected observed lines and line positions from [10] including the assignments are listed in Table 1. The detection of ammonia was not expected given the fact that the setup is optimized for ion production and the formation of ammonia from N_2 and H_2 is known to be inefficient.

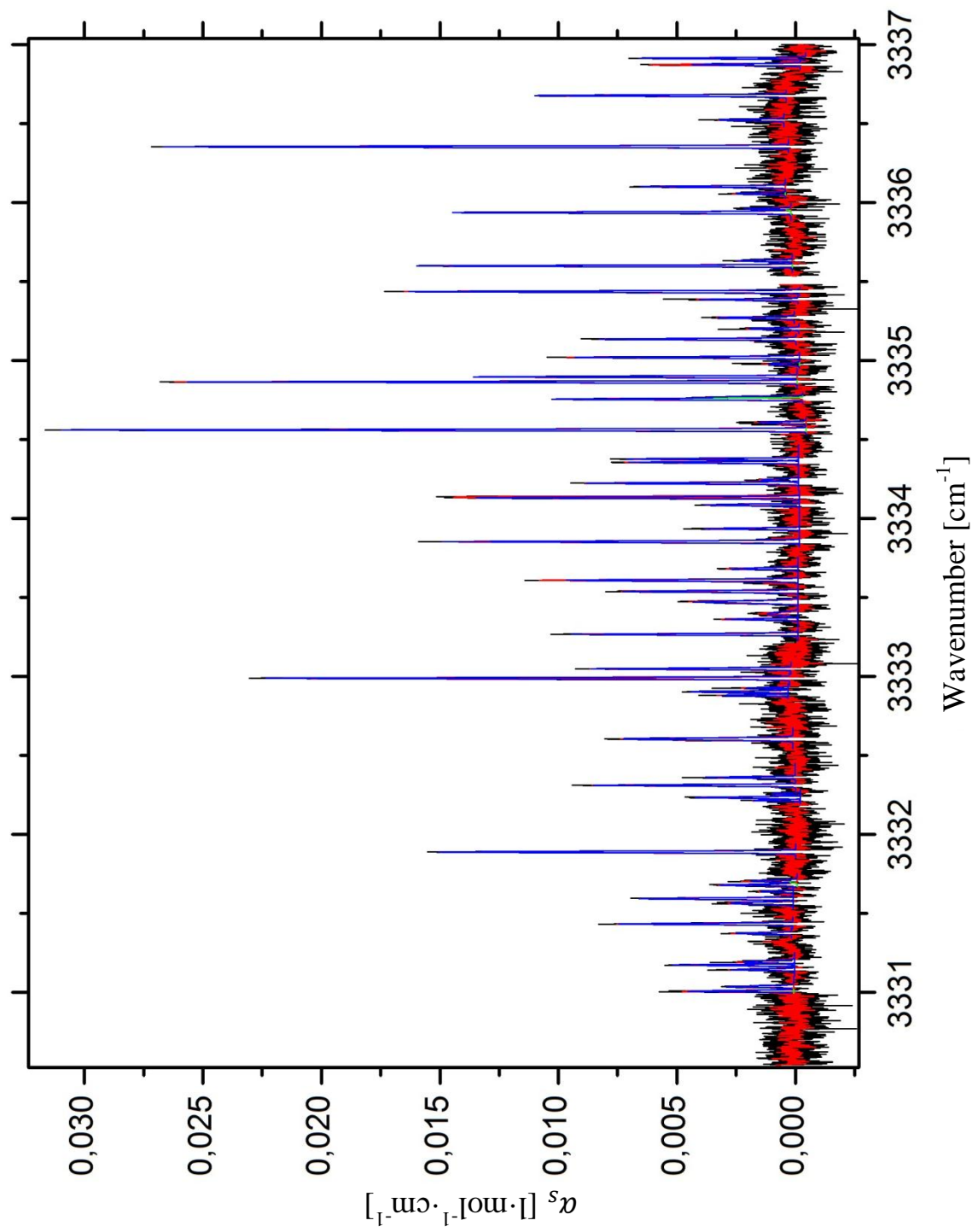


Figure 13 The spectrum from 3330,5 cm^{-1} to 3337 cm^{-1} . Each point is the average of 15 ring downs and converted to α_s , displayed in black. A 5 point adjacent average smooth is applied, displayed in red. Gaussians are fitted to the peaks in the unsmoothed data, displayed in blue.

Table 1 List of observed and literature [10] line positions with assignments. Where the first character in the Branch column indicates the vibrational parity symmetry, the second indicates the branch for the K quantum number and the third for the J quantum number. The last column indicates to which vibrational mode the transition is attributed, all vibrational transitions are from the ground vibrational state to the first excited vibrational state.

Corrected line position [$\text{cm}^{-1} \pm 3 \cdot 10^{-3} \text{ cm}^{-1}$]	Literature line position [cm^{-1}]	Branch	J	K	Mode
3336.952	3336.95178	sqQ	1	1	ν_1
3336.911	3336.91071	srP	5	0	ν_3
3336.715	3336.71601	sqQ	2	2	ν_1
3336.561	3336.56026	sqQ	2	1	ν_1
3336.391	3336.39038	sqQ	3	3	ν_1
3336.139	3336.13887	sqQ	3	2	ν_1
3336.094	3336.09453	spP	7	5	ν_3
3335.998	3336.00065	sqQ	3	1	ν_1
3335.975	3335.97588	sqQ	4	4	ν_1
3335.669	3335.66892	apP	7	5	ν_3
3335.636	3335.63575	sqQ	4	3	ν_1
3335.474	3335.47564	sqQ	5	5	ν_1
3335.423	3335.42557	sqQ	4	2	ν_1
3335.308	3335.30806	sqQ	4	1	ν_1
3335.238					
3335.173	3335.17119	aqQ	1	1	ν_1
3335.057	3335.05558	sqQ	5	4	ν_1
3335.015	3335.01274	sqQ	9	8	ν_1
3334.934	3334.93295	aqQ	2	2	ν_1
3334.902	3334.90113	sqQ	6	6	ν_1
3334.805	3334.80545	aqQ	2	1	ν_1
3334.792	3334.79249	sqQ	5	3	ν_1
3334.643	3334.64270	sqQ	5	2	ν_1
3334.598	3334.59821	aqQ	3	3	ν_1
3334.413	3334.41434	sqQ	6	5	ν_1
3334.392	3334.39309	aqQ	3	2	ν_1
3334.281	3334.27948	aqQ	3	1	ν_1
3334.261	3334.25888	sqQ	7	7	ν_1
3334.168	3334.16797	aqQ	4	4	ν_1
3334.123	3334.12327	sqQ	6	4	ν_1
3333.972	3333.97347	sqQ	6	3	ν_1
3333.890	3333.89032	aqQ	4	3	ν_1
3333.719	3333.71824	aqQ	4	2	ν_1
3333.646	3333.64439	aqQ	5	5	ν_1
3333.574	3333.57292	sqQ	7	6	ν_1
3333.508	3333.50989	sqQ	8	8	ν_1
3333.433	3333.43552	spP	8	7	ν_3
3333.398	3333.39692	sqQ	7	4	ν_1
3333.303	3333.30315	aqQ	5	4	ν_1
3333.085	3333.08621	aqQ	5	3	ν_1
3333.025	3333.02495	aqQ	6	6	ν_1
3332.963	3332.96190	aqQ	5	2	ν_1
3332.939	3332.93806	sqQ	8	6	ν_1
3332.917	3332.91581	apP	8	7	ν_3
3332.640	3332.64002	aqQ	6	5	ν_1
3332.397	3332.39832	aqQ	6	4	ν_1
3332.347	3332.34862	aqQ	7	7	ν_1
3332.293	3332.29570	aqQ	9	7	ν_1
3332.269	3332.27009	aqQ	6	3	ν_1
3332.252	3332.25386	aqQ	9	8	ν_1
3331.925	3331.92377	aqQ	7	6	ν_1
3331.740	3331.73845	aqQ	9	6	ν_1
3331.715	3331.71342	aqQ	7	5	ν_1
3331.674					
3331.629	3331.62842	aqQ	8	8	ν_1
3331.600	3331.59550	aqQ	7	3	ν_1
	3331.60475	aqQ	7	4	ν_1
3331.469					
3331.409	3331.40984	apP	6	2	ν_3
3331.228					
3331.208	3331.20783	apP	9	9	ν_3
3331.179	3331.17793	aqQ	8	7	ν_1
3331.072	3331.06815	spP	6	2	ν_3
3331.043					

When comparing the relative intensities in [10] with the measured relative intensities they appear similar. Since the measurement in [10] was performed at room temperature (297 K) this indicates the rotational temperature of the produced ammonia is of the same order of magnitude. Using [11] the rotational temperature is estimated at $300 \text{ K} \pm 30 \text{ K}$, other temperature components are also possible. As stated in chapter 3.2 this is not the expected rotational temperature of 20 K to 100 K.

To check whether lines outside the region from 3331 cm^{-1} to 3337 cm^{-1} are also caused by ammonia, Gaussians are fitted to the unsmoothed data of the survey scan. Fit parameters and assignments are given in Table 3 and Table 4 in the appendix. Most lines are assigned to be part of the P- Q- and R-branches of the $(1 \leftarrow 0)v_1$, $(1 \leftarrow 0)v_3$, or $(2 \leftarrow 0)v_4$ vibrational band.

4.3 Relative intensity measurement with added argon

If a smaller ratio of species of interest versus carrier gas is used, the cooling effect of the carrier gas in the free-jet expansion should be greater. This can be achieved by adding an inert gas like argon to the gas mixture, in this case an Ar plasma is used to which N_2 and subsequently H_2 are added.

The relative intensity of the $(1 \leftarrow 0)v_1$ aqQ(4,4), aqQ(3,3), sqQ(6,6), aqQ(2,2), and sqQ(5,5) lines was measured at gas ratios of Ar:(N_2+H_2) of 0, 2.7, 4.3, 6.6, and 7.3. No significant change in relative intensity was observed, indicating that the ratio of carrier gas versus species of interest does not affect the rotational temperature. Note that the absolute intensities did decrease as the amount of N_2 and H_2 decreased when adding more Ar to the mixture.

5. Discussion

The estimated rotational temperature of $300 \text{ K} \pm 30 \text{ K}$ in combination with the relative intensity measurement with added argon suggests that the NH_3 is not formed in the plasma and the free-jet expansion. Furthermore the average line width of $9.4 \cdot 10^{-3} \text{ cm}^{-1} \pm 0.8 \cdot 10^{-3} \text{ cm}^{-1}$ is consistent with the calculated Doppler broadening of ammonia at room temperature. Van Helden et al. [12] state that the inner surface of a vacuum chamber supports a plasma induced catalytic reaction which forms ammonia. The ammonia is subsequently desorbed from the surface, filling the vacuum chamber.

5.1 Surface catalysis

The generally accepted mechanism for generation of ammonia, the Haber-Bosch process [13], is the following: dissociative absorption of N_2 by a catalytic surface followed by stepwise recombination with absorbed and dissociated H_2 to form NH_3 with NH and NH_2 as reaction intermediates. Due to the high binding energy of N_2 (9.6 eV) the dissociative absorption of N_2 is the rate-limiting step. Usually iron or ruthenium is used as the surface catalyst. Note that this reaction does not need a plasma to occur.

According to van Helden et al. [12] the plasma is used to dissociate the precursor molecules before they come into contact with a surface. Once produced by the plasma the atomic and molecular radicals circulate through the chamber before coming into contact with a surface. The surface is then exposed to large fluxes of atomic and molecular radicals. When the surface is covered by atomic and molecular radicals it can act as a catalyst for stepwise recombination to form NH_3 . The dissociative absorption of N_2 is no longer the rate-limiting step. Note that this means that the reaction is independent of the surface material but does require the presence of a plasma to produce the atomic and molecular radicals.

According to van Helden et al. [12] the reaction for generation of NH_3 using an $\text{N}_2\text{-H}_2$ plasma to dissociate precursor molecules seems to be



Experiments carried out by van Helden et al. [12] are very similar to our experiment, however there are some differences:

- Absorption spectroscopy detection scheme and location of the laser beam with respect to the plasma source
- Injection of N_2 or H_2 into the vacuum chamber background instead of the plasma

In some experiments by van Helden et al. [12] an N_2 plasma is created and H_2 gas is injected into the background. The H_2 is dissociated by diffusing into the subsonic part of the plasma jet

and engaging in reactions with N atoms and ions created in the plasma. As for the location of the laser beam, in our case the laser is placed approximately 5 mm from the slit jet whereas in [12] the laser is placed 20 cm from the plasma source.

5.2 Outlook

To investigate the production of ammonia through surface catalysis some future experiments can be undertaken. If some amount of NH_3 is produced inside the supersonic part of the jet, it should produce a rotationally cold spectrum which is superimposed on the rotationally warm spectrum from the NH_3 produced by surface catalysis. According to van Helden et al. [12] the residence time inside the plasma is too short for NH_3 to be formed in the jet. To test this hypothesis the plasma source can be moved such that the laser no longer samples the supersonic part of the free-jet expansion. If the produced spectrum has different relative intensities such that transitions with low energy levels are less intense than in previous measurements this would indicate that some NH_3 is produced in the plasma.

A further experiment could be to make an N_2 plasma and inject H_2 into the background. Since it is very unlikely for H_2 molecules to diffuse into the supersonic part of the free-jet expansion, the dissociation of H_2 molecules cannot occur in the plasma and is only possible via reactions with N atoms or ions [12]



or



If some amount of NH_3 is produced in the plasma the rotational temperature of the spectrum should be different from previous measurements.

The search for the rotation-vibration spectrum of $\text{N}_2\text{H}^+\text{N}_2$ should be continued in combination with the search for spectra of other astrophysically relevant species such as $\text{H}_2\text{O}\cdots\text{OH}$ or $\text{OC}\cdots\text{H}^+\cdots\text{CO}$. The wavelength range of the laser system can also be changed by replacing the OPO module when looking for species like $\text{H}_2\cdots\text{HCO}^+$ or less well studied species such as $[\text{CO}]_2^+$.

$\text{H}_2\cdots\text{HCO}^+$ is interesting because HCO^+ has been observed in the interstellar medium [14] and contains hydrogen, carbon and oxygen, the building blocks of life. H_2 is the most abundant molecule in the observable universe [15] so it is likely that some $\text{H}_2\cdots\text{HCO}^+$ is present in the interstellar medium. As HCO^+ adds a dipole moment to H_2 , it could be used as a measure of H_2 abundance in the infrared in the interstellar medium.

$[\text{CO}]_2^+$ is of particular interest because it has a very high binding energy for an ionized van der Waals dimer [16]. Research on $[\text{CO}]_2^+$ has not been successful yet but it is thought to exist in the interstellar medium because CO is an abundant molecule in the interstellar medium [17].

6. Conclusion

A spectroscopic study of $\text{N}_2\text{-H}_2$ plasma products was undertaken employing CRDS. A series of transitions was observed between 3300 cm^{-1} and 3380 cm^{-1} . The densest region was near 3335 cm^{-1} . Most of the recorded lines in the region from 3331 cm^{-1} to 3337 cm^{-1} have been assigned to the ν_1 and ν_3 Q-branch of ammonia. Nearly all lines have been assigned to the P, Q, and R-branches of the ν_1 , ν_3 , and $2\nu_4$ rotational band of ammonia.

By comparing the relative line intensities to [10] and [11], the rotational temperature is estimated to be $300\text{ K} \pm 30\text{ K}$. This is not consistent with ammonia being formed in the jet since the rotational temperature should be 20 K to 100 K . The line widths are consistent with Doppler broadened ammonia at room temperature. Since the vacuum chamber walls are at room temperature, the ammonia is most likely formed via plasma induced surface catalysis as suggested by van Helden et al. [12]. Measurements using argon as a carrier gas do not indicate that the ammonia is formed in the jet.

The research set out to detect the rotation-vibration spectrum of $\text{N}_2\text{H}^+\text{N}_2$ but did not succeed, instead the rotation-vibration spectrum of ammonia was detected in an unexpected manner. The research has shown that surface catalysis reactions can account for large portions of the produced species where it was expected that all species were produced in the free-jet expansion. This needs to be taken into account in further research as any observed signals might originate from unexpected sources.

The search for $\text{N}_2\text{H}^+\text{N}_2$ should be continued when the QMS is back online, taking the abundance of ammonia into account. In the meantime interest should be shifted towards other astrophysically relevant species such as $\text{H}_2\text{O}\cdots\text{OH}$ or $\text{OC}\cdots\text{H}^+\cdots\text{CO}$. By studying these species the understanding of their chemistry increases allowing theoretical physicists and chemists to build better models and handing astronomers additional tools to determine what is going on in the interstellar medium.

7. References

- K. Terrill and D. Nesbitt. (2012) Ab initio anharmonic vibrational frequency predictions for linear proton-bound complexes OC-H⁺-CO and N₂-H⁺-N₂. *Physical Chemistry Chemical Physics*. **Vol. 12** Page 8311-8322. [1]
- A. O'Keefe and D. A. G. Deacon. (1988) Cavity ring-down optical spectrometer for absorption measurements using pulsed laser sources. *Review of Scientific Instruments*. **Vol. 59** (No. 12), page 2544-2551. [2]
- G. Berden and R. Engeln. (2009) *Cavity Ring-Down Spectroscopy, Techniques and applications*. [3]
- Tennyson, J. (2005) *Astronomical Spectroscopy, An introduction to the atomic and molecular physics of astronomical spectra*. [4]
- Wikipedia 2012, Morse potential. Consulted on 9-5-2012.
http://en.wikipedia.org/wiki/Morse_potential [5]
- R. Held. (1995). Jet Theory – Structure of a Jet Expansion. Consulted on 16-4-2012.
<http://family-held.org/website/Rudy/publications/unpublished/dossier/dos1312.htm> [6]
- The Free Dictionary (1979) Mass spectrometers. Consulted on 27-3-2012.
<http://encyclopedia2.thefreedictionary.com/Mass+Spectrometers> [7]
- P.E. Powers, Thomas J. Kulp and S.E. Bisson. (1998) Continuous tuning of a continuous-wave periodically poled lithium niobate optical parametric oscillator by use of a fan-out grating design. *Optics letters*. **Vol. 23** (No. 3), page 159 – 161. [8]
- D. Verdes, H. Linnartz, J. P. Maier, P Botschwina, R. Oswald et al. (1999) Spectroscopic and theoretical characterization of linear centrosymmetric NNH+NN. *The Journal of Chemical Physics*. **Vol. 111** (No. 18) page: 8400-8403 [9]
- A. S. Pinet and M. Dang-Nhu. (1993) Spectral intensities in the ν_1 band of NH₃. *Journal of Quantitative Spectroscopy & Radiative Transfer*. **Vol. 50** (No. 6), page 565-570. [10]
- Spectral Calc.com, line list browser. HITRAN 2008 database. Consulted on 23-5-2012.
http://spectralcalc.com/spectral_browser/db_data.php [11]
- J.H. van Helden, W. Wagemans, G. Yagci, R. A. B. Zijlmans, D. C. Schram and R. Engeln. (2007). Detailed study of the plasma-activated catalytic generation of ammonia in N₂-H₂ plasmas. *Journal of applied physics* **Vol. 101** (043305) [12]
- Wikipedia 2012, Haber process. Consulted on 19-5-2012.
http://en.wikipedia.org/wiki/Haber_process [13]
- D. Buhl and L.E. Snyder. (1970) Unidentified Interstellar Microwave Line. *Nature* **Vol. 228** page 267 – 269 [14]

G.R. Carruthers. (1970) Rocket observation of interstellar molecular hydrogen. *The Astrophysical Journal*. **Vol. 161:** L81-L85 [15]

J. Mähner, H. Baumgärtel, and K.M. Weitzel. (1995) The investigation of the $(\text{CO})_2^+$ ion by dissociative ionization of argon/carbon monoxide clusters. *Chemical Physics*. **Vol. 103:** (No. 16) page 7016 – 7024. [16]

R.W. Wilson, K.B. Jefferts, and A.A. Penzias. (1970) *The Astrophysical Journal*. **Vol. 161:** L43-L44 [17]

8. Appendix

Table 2 List of the line positions and fit parameters from the unsmoothed normal scan in the region from 3330.5 cm⁻¹ to 3337 cm⁻¹.

x_c [cm ⁻¹]	Δx_c [· 10 ⁻³ cm ⁻¹]	A [· 10 ⁻⁵ l·mol ⁻¹ ·cm ⁻²]	ΔA [· 10 ⁻⁶ l·mol ⁻¹ ·cm ⁻²]	W [· 10 ⁻³ cm ⁻¹]	ΔW [· 10 ⁻³ cm ⁻¹]
3331.0057	0.3	4.9	3	8.7	0.5
3331.0345	0.4	3.4	3	9.5	0.8
3331.1420	0.5	3.0	3	8.8	0.9
3331.1712	0.3	5.0	3	7.8	0.5
3331.1912	0.7	3.8	4	14	2
3331.3719	0.5	2.6	3	9	1
3331.4318	0.2	8.3	4	9.0	0.4
3331.5631	0.6	4.8	5	14	2
3331.5920	0.2	7.7	4	9.5	0.4
3331.6366	0.9	1.6	4	9	2
3331.6780	0.4	4.2	4	10.2	0.8
3331.7030	0.7	2.7	4	11	2
3331.8874	0.09	17.3	4	9.2	0.2
3332.2145	0.5	1.8	3	7	1
3332.2322	0.3	5.1	3	9.2	0.6
3332.2560	0.9	1.3	3	9	2
3332.3095	0.2	9.0	4	8.4	0.3
3332.3593	0.4	3.8	3	7.9	0.7
3332.6029	0.3	11.0	4	12.3	0.5
3332.8796	0.4	2.7	3	7.6	0.9
3332.9018	0.3	4.6	4	8.9	0.7
3332.9259	0.6	1.4	3	6	2
3332.9879	0.07	24.9	4	9.0	0.2
3333.0477	0.2	8.2	4	7.7	0.3
3333.2663	0.2	9.9	3	8.3	0.3
3333.3613	0.4	3.8	3	8.9	0.8
3333.395	2	3.4	5	21	3
3333.4709	0.4	8.2	4	14.8	0.7
3333.5371	0.2	9.2	3	9.2	0.3
3333.6085	0.2	12.7	3	9.3	0.3
3333.6816	0.5	3.9	3	10.7	0.9
3333.8527	0.09	17.2	3	9.1	0.2
3333.9350	0.3	4.6	3	8.8	0.6
3334.0854	0.3	4.7	3	9.3	0.6
3334.1309	0.08	16.8	3	9.2	0.2
3334.2235	0.2	10.0	3	8.4	0.3
3334.243	1	2.7	4	13	3
3334.3550	0.2	7.9	3	8.7	0.4
3334.3756	0.2	7.9	3	8.7	0.3
3334.5604	0.07	35.1	6	8.9	0.2
3334.606	2	2.8	7	11	3
3334.7550	0.3	11.8	6	8.9	0.4
3334.7683	0.6	4.4	6	9	2
3334.8645	0.07	27.4	5	8.4	0.2
3334.8969	0.2	14.7	5	8.6	0.3
3334.977	2	1.8	4	11	3
3335.0202	0.2	10.8	4	9.1	0.3
3335.1354	0.2	9.1	4	8.7	0.4
3335.2007	0.6	2.5	3	9	2
3335.2711	0.4	4.4	4	10.9	0.8
3335.3862	0.3	4.4	3	8.4	0.6
3335.4365	0.09	18.8	4	9.1	0.2
3335.5993	0.08	17.2	4	8.7	0.2
3335.6321	0.6	2.6	4	9	2
3335.9375	0.1	16.6	4	9.2	0.2
3335.9612	0.7	1.9	4	8	2
3336.0569	0.7	2.4	4	9	2
3336.1014	0.3	6.9	4	9.0	0.5
3336.3543	0.07	29.1	5	8.8	0.2
3336.5237	0.5	3.3	4	10	1
3336.6782	0.2	11.4	4	8.6	0.3
3336.8741	0.3	5.7	4	9.8	0.6
3336.9146	0.2	6.5	3	7.4	0.3

Table 3 List of the line positions and fit parameters of the unsmoothed survey scan in the region from 3300 cm^{-1} to 3380 cm^{-1} , not including the region from 3330.5 cm^{-1} to 3337 cm^{-1} .

x_c [cm^{-1}]	Δx_c [$\cdot 10^{-3} \text{cm}^{-1}$]	A [$\cdot 10^{-5} \text{l}\cdot\text{mol}^{-1}\cdot\text{cm}^{-2}$]	ΔA [$\cdot 10^{-6} \text{l}\cdot\text{mol}^{-1}\cdot\text{cm}^{-2}$]	W [$\cdot 10^{-3} \text{cm}^{-1}$]	ΔW [$\cdot 10^{-3} \text{cm}^{-1}$]
3300.574	1	1.7	4	10	3
3301.0270	0.7	1.9	4	8	2
3301.4128	0.9	2.8	4	13	2
3302.7962	0.7	1.9	3	8	2
3304.7119	2.0	3.3	6	21	4
3305.2503	0.5	3.2	4	9	2
3308.8185	0.5	2.4	3	7	1
3309.451	1	2.4	5	11	3
3309.502	1	1.5	4	9	3
3309.766	2	1.9	4	11	3
3310.6847	0.7	1.1	3	5	2
3313.7192	0.6	1.6	4	6	2
3314.111	2	2.1	5	10	3
3315.2571	0.5	5.2	5	9.3	0.9
3317.1704	0.3	7.7	5	9.2	0.6
3317.8859	0.6	4.3	5	9	2
3318.1091	0.5	4.2	5	9	2
3319.0253	0.9	2.3	6	8	2
3322.1833	0.7	2.4	5	9	2
3322.970	3	2.0	6	17	5
3323.1257	0.9	3.2	5	12	2
3323.4884	0.8	2.6	5	9	2
3323.5576	0.7	2.9	5	9	2
3327.5987	0.7	2.5	4	8	2
3328.137	2	1.4	5	10	4
3328.2345	0.7	2.2	4	8	2
3328.853	1	1.1	4	5	2
3328.893	1	2.3	6	9	3
3329.2126	0.5	7.2	7	10	1
3329.5512	0.6	3.4	5	9	2
3330.234	2.0	1.7	7	7	3
3339.4193	0.5	7.2	6	11	1
3339.8194	0.4	5.8	5	9.0	0.8
3343.0309	0.3	5.9	5	7.8	0.6
3343.6679	0.4	5.8	5	8.8	0.7
3344.3091	0.5	2.8	4	7	1
3344.359	2	2.7	5	12	3
3344.6472	0.6	3.1	5	8	2
3345.1012	0.3	10.6	7	9.4	0.6
3345.5847	0.3	7.8	6	8.2	0.6
3347.321	2	2.0	4	12	3
3348.2197	0.5	2.2	3	7	1
3348.6281	0.8	2.7	6	9	2
3352.398	1	3.1	6	10	3
3354.9631	0.8	3.3	6	9	2
3355.5263	0.6	1.5	4	6	2
3357.6031	0.7	3.3	5	9	2
3357.819	2	1.8	5	8	3
3360.8605	0.5	4.8	5	8.9	0.9
3361.2291	0.7	4.1	5	10	2
3366.8977	0.4	5.8	5	8.7	0.8
3367.4248	0.4	8.0	6	11.0	0.9
3369.6703	0.6	2.7	4	8	2
3370.1072	0.9	2.8	5	10	2
3374.5101	0.3	3.2	2	9.7	0.6
3376.2270	0.2	7.0	3	9.1	0.4
3376.2820	0.5	2.9	3	10	1
3379.3668	0.4	3.9	4	8.1	0.8

Table 4 List of observed and literature [10] line positions with assignments. Where the first character in the Branch column indicates the vibrational parity symmetry, the second indicates the branch for the K quantum number and the third for the J quantum number. The last column indicates to which vibrational mode the transition is attributed, the ν_1 and ν_3 vibrational modes are $1 \leftarrow 0$ transitions, the ν_4 mode is a $2 \leftarrow 0$ transition.

Corrected line position [$\text{cm}^{-1} \pm 3 \cdot 10^{-3} \text{cm}^{-1}$]	Literature line position [cm^{-1}]	Branch	J	K	Mode
3300.611	3300.60853	aqP	3	1	ν_4
3301.064	3301.06551	apP	9	6	ν_3
3301.450					
3302.833	3302.82942	sqR	3	3	ν_4
3304.749	3304.74829	apP	8	4	ν_3
3305.287	3305.28330	sqR	3	0	ν_4
3308.856	3308.85532	apP	10	9	ν_3
3309.488	3309.49080	apP	7	2	ν_3
3309.539	3309.53855	spP	1	0	ν_3
3309.803	3309.80152	spP	7	2	ν_3
3310.722	3310.71963	apP	9	7	ν_3
3313.756	3313.75462	apP	8	5	ν_3
3314.148	3314.15008	spP	8	5	ν_3
3315.294	3315.28878	arP	6	0	ν_3
3317.208	3317.20702	sqP	1	0	ν_1
3317.923	3317.92031	apP	7	3	ν_3
3318.146	3318.14565	spP	7	3	ν_3
3319.062	3319.06143	soQ	9	5	ν_4
3322.220	3322.22357	aqR	4	3	ν_4
3323.007	3323.00230	apP	6	1	ν_3
3323.163	3323.15897	apR	2	2	ν_4
		apP	8	6	ν_3
3323.526	3323.52452	aqR	4	0	ν_4
3323.595	3323.59409	spP	8	6	ν_3
3327.636	3327.63617	aqQ	10	9	ν_1
3328.174					
3328.272	3328.26986	sqR	4	3	ν_4
3328.891	3328.88766	srR	4	1	ν_4
3328.930	3328.92700	sqQ	9	8	ν_1
3329.250	3329.24938	aqQ	9	9	ν_1
3329.588	3329.58368	sqQ	10	9	ν_1
3330.271					
3339.456	3339.45722	apP	6	3	ν_3
3339.857	3339.85562	spP	6	3	ν_3
3343.068	3343.06896	arP	4	2	ν_3
		apP	8	8	ν_3
3343.705	3343.70516	soQ	10	9	ν_4
		spP	8	8	ν_3
3344.346	3344.34454	apP	5	1	ν_3
3344.396	3344.39568	aqR	5	1	ν_4
3344.684	3344.68368	spP	5	1	ν_3
3345.138	3345.13785	apP	7	6	ν_3
		srR	8	6	ν_4
3345.622	3345.62090	spP	7	6	ν_3
3347.358	3347.35899	aqR	5	3	ν_4
3348.257	3348.25751	apP	6	4	ν_3
3348.665	3348.66251	spP	6	4	ν_3
3352.435	3352.43789	apP	5	2	ν_3
3355.000	3355.00082	aqR	0	0	ν_1
		apP	7	7	ν_3
3355.563	3355.56552	spP	7	7	ν_3
3357.640	3357.64868	arP	4	0	ν_3
3357.857	3357.86235	spP	6	5	ν_3
3360.898	3360.90108	apP	5	3	ν_3
3361.266	3361.27504	spP	5	3	ν_3
3366.935	3366.94297	apP	6	6	ν_3
3367.462	3367.46994	spP	6	6	ν_3
3369.707	3369.71152	apP	5	4	ν_3
3370.144	3370.14901	spP	5	4	ν_3
3374.547	3374.55125	aqR	1	1	ν_1
3376.264	3376.26961	sqR	1	0	ν_1
3376.319	3376.32579	sqR	1	1	ν_1
3379.404	3379.41095	spP	5	5	ν_3